**PAPER** • **OPEN ACCESS**

# Application of the tomographic BOS technique to a H2-air premixed flame

To cite this article: F. Iapaolo *et al* 2024 *J. Phys.: Conf. Ser.* **2802** 012012



Journal of Physics: Conference Series **2802** (2024) 012012 doi:10.1088/1742-6596/2802/1/012012

# Application of the tomographic BOS technique to a H2-air premixed flame

**F. Iapaolo, F. Cozzi and M. Orlando**

Politecnico di Milano, Dipartimento di Energia, Via Lambruschini 4, Milano, Italy

E-mail: francesca.iapaolo@polimi.it

**Abstract**. Background Oriented Schlieren (BOS) is a line of sight optical (LoS) technique used for visualizing and measuring density gradients in transparent media by exploiting the fluid density and refractive index relationship. This study applies BOS to a premixed axis-symmetric hydrogen flame, aiming to quantitatively estimate its density and temperature distributions using the ARAP (Arbitrary Ray Axisymmetric Projection) deconvolution algorithm. The BOS technique consists in acquiring images of a background with and without the flame; light rays passing through the flame are deflected due to the heterogeneous refractive index field. Cross-correlation algorithms are then employed to quantify these deflections. The ARAP transform is preferred to Abel-based methods because it models light rays as converging to a single point according to the pinhole camera model. Assuming constant composition, density gradients are evaluated, and considering ideal gas behaviour and constant pressure, the temperature distribution is estimated. The study explores the influence of parameters like regularization and integration steps for the ARAP transform. Consistency analysis involves evaluating temperature trends at various flame heights and comparing them with thermocouple measurements. Additionally, a preliminary estimation of tomographic BOS uncertainties is provided.

## 1. Introduction

Background Oriented Schlieren (BOS) imaging is currently an effective technique for qualitative and quantitative fluid measurement [1]. It is widely used to investigate different physical phenomena such as compressible flows and shock waves [1,2,3,4,5], thermal boundary layer [6,7,8], combustion processes [9,10,11,12] etc. and it is commonly used to visualize density gradients generated by temperature, pressure or chemical composition gradients. The BOS technique visualizes density gradients by capturing an image of an object within a medium of varying density, which appears distorted due to light refraction. By comparing the distorted image with the one taken in the absence of the varying density medium (i.e. the undistorted image) the amount of light refraction, and thus the density gradients, can be quantified. The simple optical set-up required by the BOS imaging, basically just a lens, makes it cheaper and faster to align than the classical schlieren one [13,14], furthermore the quantitative amount of light refraction is easily recovered by comparing distorted and undistorted images through cross-correlation algorithms [15] or either optical flow [16] and dot tracking methods [17]. Besides density and temperature, also flow velocity can be inferred by analyzing the BOS images [18]. When dealing with 3D schlieren objects, a tomographic approach is required to recover the local density from the BOS image. For axisymmetric schlieren objects, BOS images taken along a single view direction orthogonal to the flow axis are sufficient to recover the density by using the Abel

inverse transform. For example, this technique has been applied to investigate the supersonic flow around cones [1,18,19] or jet flows [20,21]. On the other side, tomographic reconstruction of 3D and not axisymmetric schlieren objects requires several BOS distortion map fields obtained along various viewing directions, as for example done in Atcheson et al. [16] and Nicolas et al. [3].

The Abel inverse transform assumes parallel projecting rays, which may not be the case when using entocentric lenses and a short object-to-lens distance. Recently, Sipkens et al. [23] have developed the Arbitrary Ray Axisymmetric Projection (ARAP) transform, an Abel inversion method that relaxes this assumption and assumes diverging light rays originating from a single point. He demonstrated that this approach reduces errors in tomographic reconstruction by applying it to a simulated BOS scenario.

The aim of this work is to explore the possibility of estimating the temperature field of a Bunsen premixed hydrogen-air flame using tomographic BOS, employing the novel ARAP transform. The resulting temperature distribution is compared to that obtained through two Abel-based methodologies: the direct two-point (2pt) [24] and the indirect Onion Peeling (OP) [25] approach. Additionally, a thorough investigation is conducted to determine how the regularization parameter and discretization grid size affect the tomographic results. Furthermore, the temperatures measured by the tomographic BOS technique are compared with thermocouple measurements. To assess the reliability of the tomographic results, a simplified uncertainty analysis is eventually performed.

## 2. Tomographic BOS

Background Oriented Schlieren (BOS) is part of the broader family of schlieren techniques, including schlieren imaging, schlieren photography, and schlieren tomography. These are optical techniques used to visualize density variations in transparent media, such as gases or liquids. One of the main advantages of BOS is its non-intrusive nature as it eliminates the need for introducing a probe that could potentially perturb the flow. BOS is commonly used in aerodynamics and fluid dynamics research to study the behavior of air flows around objects and has been widely applied to investigate phenomena such as shock waves [4,23], boundary layers [6,23], gas flames [9,10] and turbulence [16].

In a typical BOS setup, the transparent medium is placed between a camera and a background, often characterized by a random speckle pattern. In BOS analysis the quality of the result is highly affected by the choice of the background pattern which must be bigger than the observed phenomenon and must be characterized by a random pattern [27].

The camera is used to acquire images of the background pattern as seen through the inhomogeneous transparent medium. The captured images appear distorted because light rays are deflected by a quantity that is proportional to refractive index gradients $n$ as per equation (1):

$$\varepsilon_y(y) = \frac{1}{n_0} \int \frac{\partial n(r)}{\partial y} ds \tag{1}$$

where $\varepsilon_y$ represents the light-ray deflection in horizontal direction and $n_0$ is the ambient refractive index [14,25].

Changes in the refractive index may be caused by pressure, temperature and composition changes along the light ray path according to the Gladstone-Dale equation (2), valid for ideal gas mixtures [29]:

$$n_{mix} = 1 + \frac{p}{RT} R_{G_{mix}} \tag{2}$$

where $p$ is the pressure, $T$ is the temperature, $R$ is the universal gas constant, $R_{G_{mix}} = \sum_{i=1}^{N} R_{G_i} x_i$ is the Gladstone-Dale constant for the mixture, $R_{G_i}$ is the Gladstone-Dale constant at wavelength $\lambda = 633\ nm$ of the i-th species and $x_i$ is the molar fraction of the i-th species.

To quantify the image distortion, either cross correlation or optical flow algorithms [14,23] can be applied to BOS images.

The displacement maps resulting from the image processing represent the integral of the ray deflection occurring along the ray path. Thus, for a 3D schlieren object, a tomographic approach needs to be implemented if the spatial distribution of the refractive index is sought, which requires BOS

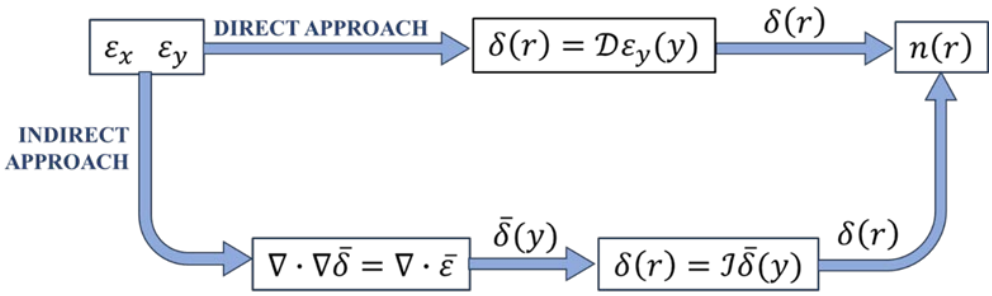


**Figure 1.** Schematic representation of different deconvolution strategies with direct and indirect approaches.

images taken from different points of view. On the other hand, for axisymmetric objects such as the flame under study, the 2D refractive index field can be obtained through the inverse Abel transform in equation (3), along with BOS images taken from a single viewpoint.

$$\delta(r) = -\frac{1}{\pi}\int_r^\infty \varepsilon_y \frac{dy}{\sqrt{y^2-r^2}} \tag{3}$$

Usually, equation (1) is rewritten by introducing $\delta$, equation (4), and performing a change of variable to obtain equation (5):

$$\delta(r) = \frac{n(r)}{n_0} - 1 \tag{4}$$

$$\varepsilon_y(y) = \frac{1}{n_0}\int \frac{\partial n(r)}{\partial y} ds = \int \frac{\partial \delta(r)}{\partial y} ds = \frac{\partial}{\partial y}\int \delta \, ds = \frac{d\bar{\delta}(y)}{dy} \tag{5}$$

where $\bar{\delta}$ represents the integrated $\delta$ along the light path $s$.

There are two main solution strategies commonly implemented to compute $\delta$ from deflection angles $\varepsilon$, **figure 1**. The first one is the direct approach and computes $\delta$ directly from the deflection angles. On the contrary, in the indirect approach $\bar{\delta}$ is determined first by solving a Poisson equation, then an inversion algorithm is applied to compute $\delta$. Both direct and indirect approaches use the inverse Abel transform and model light-rays as parallel to the optical axis of the camera. This condition is fulfilled when using telecentric lenses but may not be the same for the commonly used entocentric lenses for which light-rays converge at a single point. Using entocentric lens, the closer the camera is to the background, the more divergent the light rays become, leading to inaccurate results. In this study, the Arbitrary Ray Axisymmetric Projection (ARAP) transform proposed by Sipkens et al. [23] is applied, since it generalizes the Abel transform by modelling light-rays as straight lines converging at a point. Differently from Abel-based approaches, the ARAP transform does not require to exactly identify the position of the axis of symmetry and is characterized by a higher numerical stability.

Sipkens et al. [23] suggest modelling light rays passing through the ASO as straight lines, see **figure 2**, described by the general equation (6):

$$y = m_y z + y_0 \tag{6}$$

In this case, the ARAP transform is formulated using a direct approach leading to a kernel [23] of the form in equation (7):

$$K = \frac{2}{1+m_y^2}\frac{r_h}{(r^2-r_h^2)^{1/2}} \tag{7}$$

where $r_h$ represents the minimum distance between the ray and the origin of the $x\,y$ axis, which coincides with the centre of ASO:

$$r_h = \frac{y_0}{(1+m_y^2)^{1/2}} \tag{8}$$

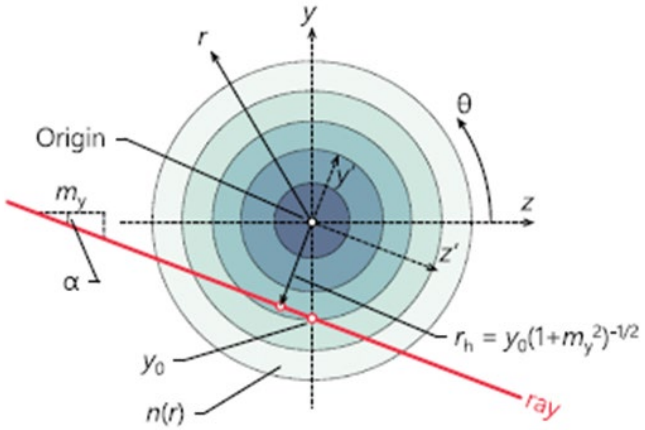


**Figure 2.** Coordinate system for the ARAP transform used in projecting deflectometry measurements of an Axisymmetroc Schlieren Object (ASO) onto the camera sensor [23].

The ARAP algorithm is derived using a Bayesian approach and the solution $\bar{\delta}$ is computed by minimizing the expression reported in square backets in equation (9):

$$\bar{\delta} = argmin_{\delta}[\|\mathbf{L}_e(\boldsymbol{\varepsilon} - \mathbf{D}\delta)\|^2 + \|\lambda \mathbf{L}_{tk}\delta\|^2] \quad (9)$$

where $\mathbf{L}_e$ is the matrix square root of the error covariance matrix, $\boldsymbol{\varepsilon}$ represents the measured deflections, $\mathbf{D}\delta$ represents the deflections predicted by the forward model and $\mathbf{D}$ is the discretization matrix of the kernel $K$ depending on light-rays equations (thus $y_{0,i}$ $m_{y,i}$), $\lambda$ is the regularization factor, $\mathbf{L}_{tk}$ represents the Tikhonov matrix. Further details regarding each term can be found in the article [23].

The ARAP algorithm, needs the specification of the following parameters:

- The regularization parameter $\lambda$ which is used to smoothen the solution.
- The discretization step $N_r$ and $N_x$ which represent the number of annuli and slices used to divide the ASO. The maximum $N_x$ which can be set is the number of rows of the deflections matrix; while the maximum $N_r$ coincides with half of the number of columns of the deflections matrix.
- The focal length and the sensor size that are used to model the camera according to the pinhole model.
- The position of the camera with respect to the ASO.

Sipkens et al. [23] suggest choosing the regularization factor by applying the ARAP transform to a synthetic well-known ASO and by comparing the results with the synthetic map. The regularization factor leading to lower residuals is chosen as the one to be used in the algorithm. In our case it is not possible to follow this advice since the temperature map of the premixed air-hydrogen flame is not known. For this reason, a sensitivity analysis should be performed; the results can be found in section 5.

Finally, considering that it is not possible to run the algorithm setting the minimum integration step due to the high computational cost, a sensitivity analysis aiming to the study of the filtering effect on the results is performed to choose properly $N_r$ and $N_x$.

## 3. Experimental setup

**Figure 3a** shows the BOS experimental setup which is composed by a 9.7” LCD monitor and a Hamamatsu C8484-05 CCD camera mounted on the same optical rail by means of two rail carriages to ensure a precise and fast position adjustment, while the Bunsen burner is located between the camera

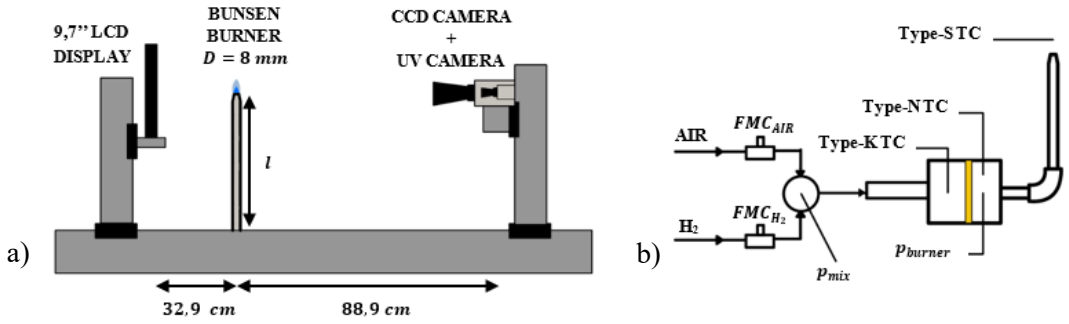


**Figure 3.** a) BOS experimental setup and b) gas supply system on the right.

and the display. The latter is at a distance of $121.8\,cm$ from the Hamamatsu and $32.9\,cm$ from the burner. The monitor has a resolution of $2048\,x\,1536\,pixels$ with a pixel pitch of $96\,\mu m$ and a contrast ratio of 1000:1. The CCD camera has a resolution of $1344\,x\,1024\,pixels$ and a pixel pitch of $6.45\,\mu m$ and it is equipped with a $100\,mm$ lens. The camera is focused on the monitor which is used to display the background image.

Flame monitoring and UV imaging are performed by a $6.3\,MP$ camera equipped with a $75\,mm$ $f/3.8$ ultraviolet lens together with a Near-UV Bandpass Filter ($315-365\,nm$). Both cameras are placed at the same distance from the LCD monitor.

The Bunsen-type burner is a cylindrical stainless-steel tube measuring $8\,mm$ in diameter and $40\,cm$ in length. The fuel-air supply system is shown in **figure 3b**; the air and hydrogen flow rates are set by means of two thermal mass flow meters/controllers. The air and hydrogen mixture arrives in a cylindrical settle chamber where a porous septum (yellow element in **figure 3b**) is located, the septum laminarizes the flux and acts effectively as a flashback arrestor. A type-N thermocouple downstream the porous septum allows to detect the flashback occurrence, while a type-K one measures the gas mixture temperature upstream of the septum. The flame is ignited by an electric igniter placed close to the burner rim. A type-S thermocouple, with a junction diameter of $0.75\,mm$, placed on a micrometric translational glide mechanism allows to measure the gas temperature at different radial and axial positions of the flame.

The experimental tests are carried out at a thermal power $P_{th}$ of $1\,kW$, equivalence ratio $\phi_{eq}$ of 0.45 and the corresponding flowrates and their uncertainties are reported in **table 1**.

**Table 1.** Experimental flowrates and corresponding uncertainties.

| | Flowrate $[nl/min]$ | Uncertainty $[nl/min]$ |
|---|---|---|
| **Air** | 30.0 | $\pm 0.65$ |
| **Hydrogen** | 5.6 | $\pm 0.18$ |

The corresponding Reynolds number $Re = 5578$ is computed using the bulk velocity and the inner diameter of the Bunsen burner as characteristic length. The mixture dynamic viscosity $\mu_{mix}$ used for Reynolds number computation is obtained by applying the formula proposed by T. A. Davidson [30] valid for air-hydrogen lean mixtures in (10):

$$\mu_{mix} = \frac{\sum_{i=1}^{N} \mu_i x_i \sqrt{MM_i}}{\sum_{i=1}^{N} x_i \sqrt{MM_i}} \tag{10}$$

where $\mu_i$, $x_i$ and $MM_i$ are the dynamic viscosity, the molar fraction and the molar mass of the i-th species, respectively.

## 4. Data acquisition and analysis

The background pattern used during the experimental campaign is visualized by the LCD monitor and is composed by an image of randomly distributed white particles, in the recorded image each particle has a diameter of about 2.5 $pixels$ and the particle density results to be about $0.034\ particles/pixel$.

The particle distribution is obtained by dividing the background image on the LCD monitor into a regular grid of $4x4\ pixels$ areas, just one particle with a random position is collocated in each area, this prevents particle to overlap while obtaining at the same time a random particles distribution. The brightness of the particle pixels is assigned accordingly to a truncated Gaussian distribution.

During the experimental campaign, a total of 100 background images have been acquired with the hydrogen flame, and one image without the flame has been taken as the reference undistorted background image. The density variation occurring in the flame, originated by the change in composition and temperature, deflects the light rays, distorting the image of the background [10]. To convert the measured displacements from pixels to millimeters, a camera calibration is carried out using a pinhole model and a chessboard image visualized by the LCD monitor. All images are acquired with a lens aperture of $f/22$ and an exposure time of $64000\ \mu s$.

Images are processed by a commercial software (DynamicStudio 7.3); they are first dewarped, and then a multi-pass cross-correlation analysis is applied with a final interrogation area of $8x8\ pixels$ with an overlap of 75% on both the horizontal and vertical directions. Peak validation is carried out by enforcing a S/N ratio of 1.5 and a peak height of 0.70. Eventually, the 100 displacement maps are averaged together to obtain a single mean displacement.

Assuming small deflection angles, it is possible to compute deflections in the $x$ and y directions from the corresponding measured displacements $\Delta x$ and $\Delta y$ (11):

$$\varepsilon_x \sim \frac{\Delta x}{Z_d} \qquad \varepsilon_y \sim \frac{\Delta y}{Z_d} \tag{11}$$

where $Z_d$ represents the distance between the background and the axis of the Bunsen burner [31].

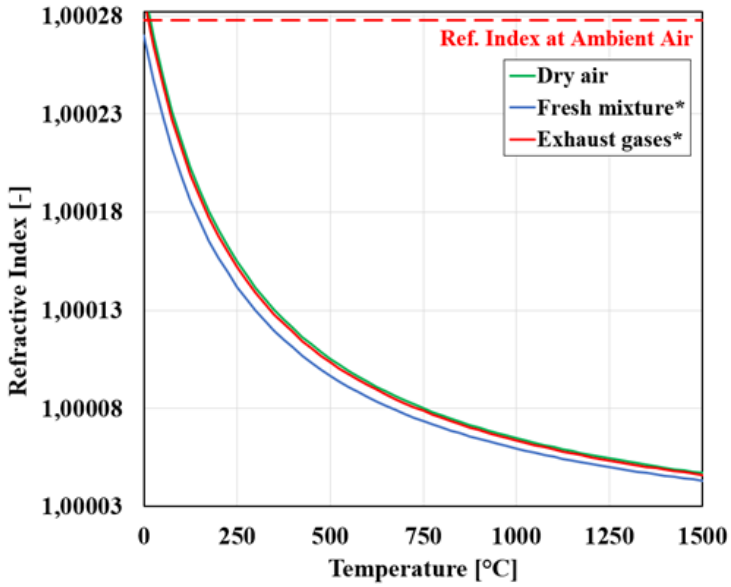


**Figure 4.** Refractive index trends as function of temperature for three gaseous mixtures: air, fresh mixture (air and hydrogen), exhaust gases (water vapour, oxygen and nitrogen). *Values computed assuming complete combustion at $\phi = 0.45$.

Starting from deflection, the non-dimensional parameter $\delta$ is computed using the ARAP transform and the refractive index field is obtained by inverting equation (4) and setting the air refractive index equal to $n_0 = 1.00026794$. The value of $n_0$ is estimated at $\lambda = 633\,nm$ using equation (2) by imposing $p = 1\,atm$, $T = 25°C$ and considering dry air with a molar composition of 21% $O_2$ and 79% $N_2$ [32].

Eventually, the density is computed by inverting the Gladstone-Dale equation [29] as per equation (12):

$$\rho = \frac{\delta n_0}{RG_{mix}} \tag{12}$$

where $\rho$ is the molar density. As indicated by equation (12), the refractive index, denoted as $\delta$, is determined by both gas composition and temperature. However, the temperature has a significantly greater impact on $\delta$, compared to gas composition, as illustrated in **Figure 4**. This plot demonstrates the dependence of the refractive index on temperature for three different gas mixtures: ambient air, fresh mixture (hydrogen-air), and exhaust gases. The refractive index of the mixture is calculated using formula (2); with the composition of the exhaust gases assumed based on complete combustion due to the very lean flammable mixture.

The resulting refractive indexes for dry air and exhaust gases are nearly identical due to the high molar concentration of nitrogen in both mixtures. In contrast, hydrogen in the fresh mixture causes a shift in the curve towards lower refractive index values. **Figure 4** indicates that temperature variations exert a greater influence on the refractive index than variations in mixture composition. This suggests that temperature is the primary parameter influencing the variation of $n_{mix}$. Due to this factor, the Gladstone-Dale constant is regarded as unaffected by the composition of the mixture, maintaining a constant value equivalent to that of ambient air. $R_{G\,mix} = R_{G\,air} = 6.55544\ cm^3/mol$ [29].

Once the density field is known, the temperature distribution is estimated by assuming ideal gas behaviour as per equation (13):

$$T = \frac{p}{R\rho} \tag{13}$$

## 5. Results

### *5.1. Displacement Maps*

The mean displacement map, **figure 5**, indicates an axisymmetric behaviour with maximum values located in proximity to both the flame front and the plume contour. Where the former corresponds to the boundary between the fresh mixture and the exhaust gases area, and the latter is the region where the combustion products mix with the surrounding fresh air. The three horizontal red lines in **figure 5** show the heights ($h = 0.6D, h = 1.2D, h = 3D$ measured with respect to the Bunsen rim) at which the displacement components, the refractive index and the temperature profiles are extracted.

Being the flame axisymmetric, the mean radial and vertical displacement profiles show an antisymmetric (**figure 6a)** and a symmetric (**figure 6b**) behaviour, respectively, with respect to the burner axis. Consequently, only the region to the right of the burner axis is discussed, and similar considerations apply to the left side as well.

Considering the profile of the radial displacement at the lowest height $h = 0.6D$, **(figure 6a)**, and moving from the burner axis outwards, the displacement rapidly goes from zero to its maximum value, located at about $x/D = 0.22$. This behaviour can be attributed to the strong density gradient originated by the temperature increase occurring upstream of the flame front. Then, the radial displacement reaches its minimum value ( $|\Delta_x| \sim 0.297\ mm$ ) at about $x/D = 0.69$, nearby the plume contour; here hot exhaust gases meet ambient air, leading to a high-density gradient. Finally, the displacement reaches a zero value with a steep slope, as light rays are passing through ambient air without undergoing refraction. By moving downstream, the magnitude of the maximum radial displacement decreases and its radial position moves closer to the burner axis following the conical shape of the premixed flame.

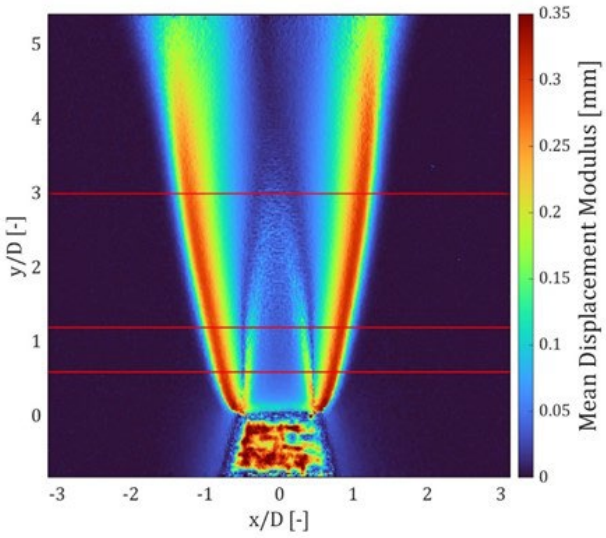


**Figure 5.** Mean displacement modulus map. Red lines show extraction heights at which profiles of displacement, refractive index and temperature are extracted.

At $h = 3D$ and close to the burner axis, the radial deflection of the light rays is quite small, and its maximum has almost disappeared. This occurs because the light rays and the refractive index gradient are almost parallel to each other there. Instead, the larger plume contour brings the minimum displacement values at farther radial distances.

**Figure 6b** illustrates the mean vertical displacement profiles. Despite exhibiting sensible noise, the profiles are distinctly characterized by two outer peaks and two inner ones located almost at the same positions of the maximum and minimum peaks of the radial displacement, respectively. The maximum vertical displacement $\Delta_y \sim 0.075\ mm$ occurs at $h = 0.6D$. Moving downstream, the magnitude of the peaks diminishes, and simultaneously, the two inner peaks approach the burner axis due to the conical shape of the flame front. Conversely, the outer peaks shift outward as the flame plume enlarges.

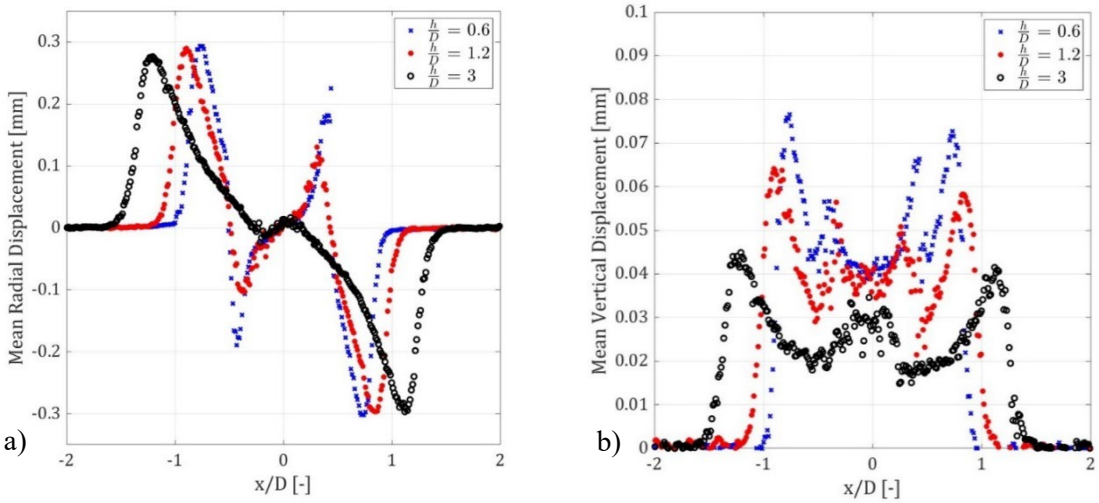


**Figure 6.** a) Mean radial displacement profiles extracted at $h = 0.6D, h = 1.2D, h = 3D$ from the burner rim; b) Mean vertical displacement profiles extracted at $h = 0.6D, h = 1.2D, h = 3D$ from the burner rim.

*5.2. Refractive index distribution*

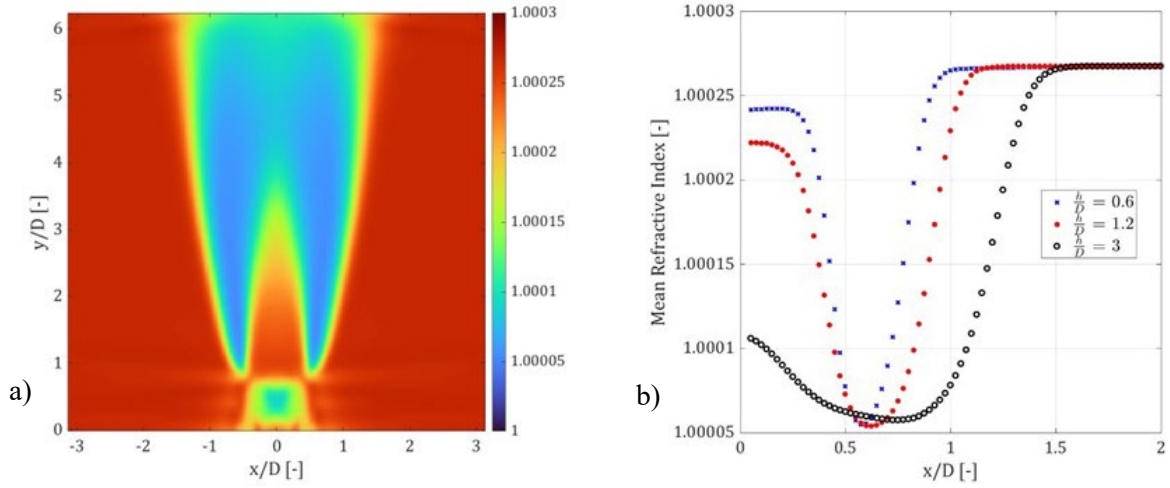


**Figure 7.** a) refractive index field obtained by setting $N_r = 125, N_x = 250$ and $\lambda = 75$; b) refractive index profiles extracted at $h = 0.6D, h = 1.2D, h = 3D$ from the burner rim.

The refractive index field illustrated in **figure 7a** is obtained inverting equation (3) and setting the ARAP parameters $N_r = 125, N_x = 250$ and $\lambda = 75$. The ARAP transform yields an axisymmetric map, thus, only the right half of the refractive index profiles is shown in **figure 7b**. At the extraction heights $h = 0.6D$ and $h = 1.2D$, moving along the radial coordinate from $x/D = 2$ to the symmetry axis, the refractive index goes from $n = 1.00026794$ in the ambient to a minimum at $x/D = 0.6$ in the flame region. Then, the profile rises and settles at a value below ambient air within the flame cone, primarily due to the presence of hydrogen, which has a lower refractive index than air. A similar trend is observed at $h = 3D$, but refractive index is lower almost at every radial position due to the diminishing presence of fresh mixture; the minimum shifts at higher radial coordinate $x/D = 0.8$ as flame plume is enlarging.

*5.3. Temperature distribution*

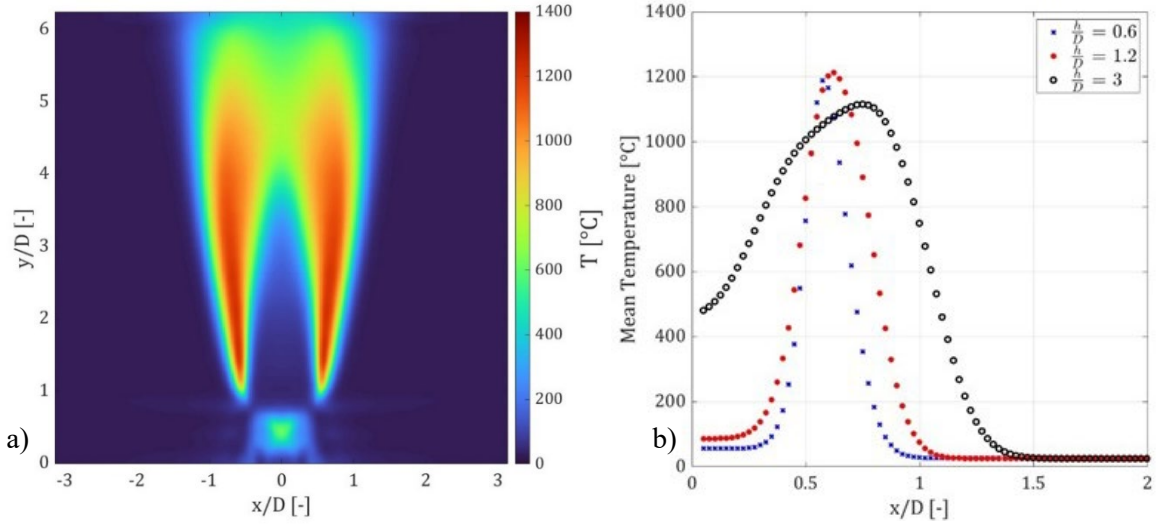


**Figure 8.** a) temperature field obtained from data of **figure 7**; b) temperature profiles extracted at $h = 0.6D, h = 1.2D, h = 3D$ from the burner rim.

The temperature distribution reported in **figure 8a** is estimated with equation (7) and radial profiles extracted at flame heights of $h = 0.6D, h = 1.2D, h = 3D$ are shown in **figure 8b**. At lower heights, specifically at $h = 0.6D$ and $h = 1.2D$, temperatures near the burner axis are slightly higher than ambient due to both variations in mixture composition and temperature. Furthermore, the temperature profile at $h = 1.2D$ indicates higher temperatures than that at $h = 0.6D$, implying that inward reaction heat flux coming from the flame front is preheating the fresh mixture. At higher radial coordinates, temperature increases with a steep gradient and reaches a maximum at about $x/D = 0.6$ in the burnt gases region; this value is almost comparable with the theoretical adiabatic flame temperature $T_{ad} = 1265°C$. Then, the trend reverses till reaching the temperature of the surrounding ambient outside the flame plume area. Moving downstream at $h = 3D$, the trend shows a reduction in the maximum temperature magnitude, with the peak temperature located at a higher radial coordinate according to the shape of the flame plume.

### *5.4. Influence of ARAP parameters*

The influence of the regularization parameter $\lambda$ is shown in **figure 9a** and **figure 9b** where the radial temperature profiles at $h = 0.6D$ and $h = 1.2D$ are plotted for different values of $\lambda = [5, 25, 50, 75, 100, 125]$. As $\lambda$ values increase, both the maximum temperature and the curve slope reduce.

This effect is more pronounced at lower flame heights, where gradients are stronger and the regularization parameter $\lambda$ effectively acts as a filter, attenuating the sharp variations in the temperature. The choice of the $\lambda$ parameter is driven by a trade balance between achieving a smooth solution and limiting the filtering effect.

**Figure 9c** and **figure 9d** illustrate the effect of the grid of integration. The discretization of the integration grid, which dimensions are $N_r \times N_x$, determines the number of rays that intersect the axisymmetric object. The number of elements of the grid significantly affects the resolution of the

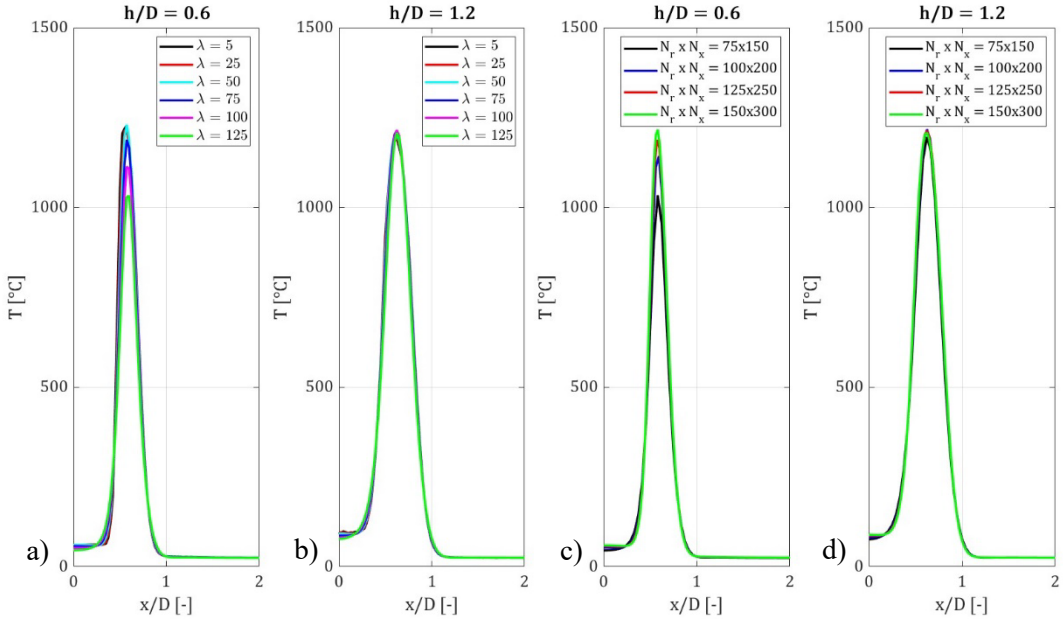


**Figure 9.** Temperature profiles extracted at a) $h = 0.6D$ and at b) $h = 1.2D$ (b) from the burner rim, obtained adopting various regularization parameter $\lambda$ and setting $N_r = 125, N_x = 250$. Temperature profiles extracted at c) $h = 0.6D$ and at d) $h = 1.2D$, obtained adopting various integration grids ($N_r \times N_x$) and setting $\lambda = 75$.

outcome and the computational effort. The graphs reveal that the choice of the integration grid is crucial in the regions featuring strong gradients, especially at lower heights. In such regions, the adoption of a raw grid (i.e. low values of $N_r$ and $N_x$) implies loss of information. This effect can be appreciated in **Figure 9c** where the raw-grid curves underestimate temperature peak value. From **figure 9c** and **figure 9d** it is evident that to obtain optimal resolution while mitigating the computational effort can be accomplished by adopting an integration grid with approximately half of elements of the displacement map. In this case, using $N_r = 125$ and $N_x = 250$ appears to be sufficient as the displacement map has $512 \times 512$ elements.

*5.5. Comparison with Abel and thermocouple measurements*

**Figure 10** depicts the comparison of mean radial temperature profiles obtained using the ARAP method at different heights from the burner rim, alongside profiles obtained using the 2pt [24] and onion peeling (OP) [25] Abel-based methods, as well as thermocouple measurements. Since Abel-based methods 2pt and onion peeling produce two different maps for the right and the left halves of the image, the curves reported in **figure 10** are averaged between these two halves.

The 2pt profile follows closely the ARAP curve for all heights. However, at $h = 3D$ it exhibits some noise compared to the ARAP profiles. This effect may be attributed to the absence of a regularization factor in the 2pt algorithm. On the contrary, the onion peeling curve is misaligned with both the ARAP and the 2pt curves. Specifically, at $h = 0.6D$ and $h = 3D$ the onion peeling respectively overestimates and underestimates the outcome of both ARAP and the 2pt. This discrepancy may be due to the Poisson integration employed in the onion peeling technique. It is important to notice that at $h = 0.6D$ the maximum temperature computed with the OP (about $1400°C$) is not consistent with the adiabatic flame temperature $T_{AF} = 1265°C$ computed with Cantera at $\phi_{eq} = 0.45$.

The thermocouple measurements are performed at steady-state conditions at heights $h = 0.6D$, $1.2D$ and $3D$. At $h = 0.6D$, **figure 10a**, the temperatures measured by the thermocouple are significantly different from the temperature profiles obtained from BOS. The differences might be related to the thermocouple size which is too large to accurately measure the temperature distribution

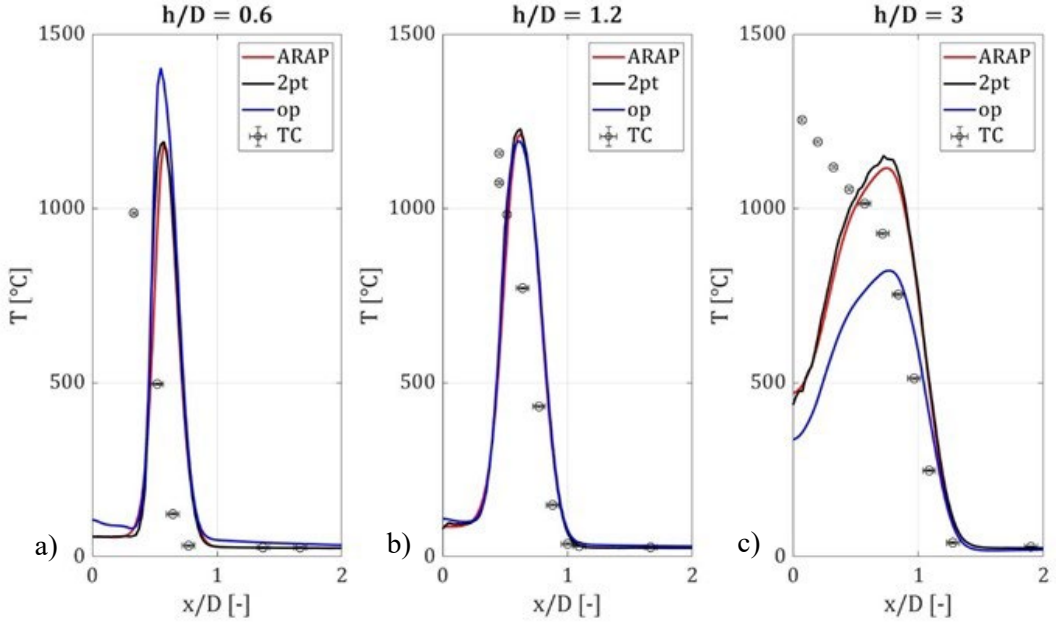


**Figure 10.** Thermocouple measurement and ARAP, 2pt and onion peeling temperature profiles extracted at a) $h = 0.6D$, b) $h = 1.2D$ and c) $h = 3D$ from the burner rim. Plots obtained setting $N_r = 125, N_x = 250$ and $\lambda = 75$.

in that region. At flame heights equal to $h = 1.2D$ and $h = 3D$ and for $x/D > 0.5$, **figure 10b** and **figure 10c**, the thermocouple measurements closely match the temperature profiles obtained from BOS, displaying almost identical trends. However, the thermocouple measurements are consistently lower than those obtained from BOS at each radial coordinate. In the fresh mixture region, i.e. at about $x/D < 0.5$ the temperature measured by the thermocouple increases continuously as we move toward the burner axis; conversely, the temperature profile from BOS decreases rapidly. Such different trend between the two is likely due to catalytic effect of the platinum thermocouple triggered when the thermocouple moves into the region inside the flame cone and occupied by the fresh mixture. At $h = 3D$, **figure 10c**, the higher temperature measured by the thermocouple may be attributed to a combined catalytic effect and the fluctuations in the flame cone tip caused by turbulence, which alternately expose the thermocouple to burnt and fresh gases, resulting in higher temperature readings. On the other hand, the ARAP results are based on a time-averaged displacement map, which mitigates the temperature fluctuations caused by flame tip oscillation.

## 6. Uncertainties

A simplified analysis of the uncertainty on the tomographic BOS temperature measurements is conducted by considering three main contributions**:** the uncertainty in the distance between the Bunsen burner and the background, $\varepsilon_{Z_d}$, the statistical uncertainties in the mean displacement map, $\varepsilon_{\Delta X}$ and $\varepsilon_{\Delta Y}$, and the assumption of a constat gas composition, i.e. a constant $R_G$. The total uncertainty is determined by combining the uncertainties associated with these terms using the error propagation method [33].

The uncertainty in the distance $Z_d$, denoted as $\varepsilon_{Z_d} = 1\,mm$, affects the value of the deflection computed through equation (11). Its impact on the BOS temperature measurements is quantified for the case depicted in **figure 5** and shown in **figure 11,** where the percentage difference between the temperature values obtained using $Z_{d,ref} = 329\,mm$ (the reference case) and $Z_d = Z_{d,ref} \pm \varepsilon_{Z_d}$ is reported.

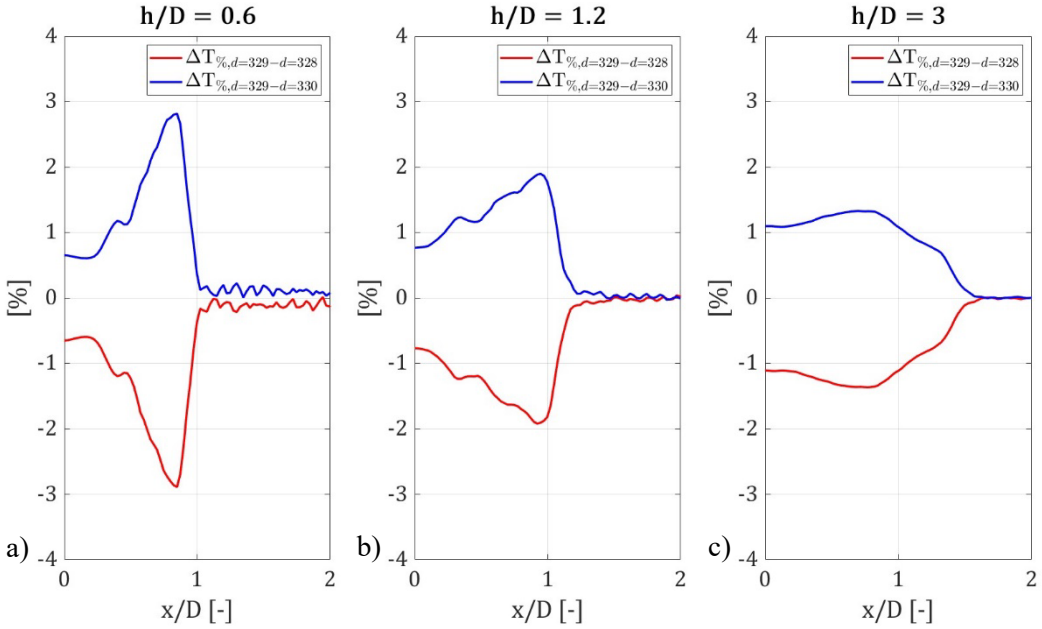


**Figure 11.** Temperature percentage difference between the reference case $Z_d = 329\,mm$ and the shifted cases $Z_d = 328\,mm$ and $Z_d = 330\,mm$ extracted at a) $h = 0.6D$, b) $h = 1.2D$, c) $h = 3D$ from the burner rim.

An increase in the distance $Z_d$ leads to smaller deflections, resulting in lower computed temperatures compared to the reference case. Conversely, a decrease in the distance corresponds to higher computed temperatures due to increased deflection magnitudes. The maximum percentage difference, below 3% at $h = 0.6D$, corresponds to a maximum temperature uncertainty of approximately $\varepsilon_{\Delta T}^{Z_d} = 35°C$, and is located in the burnt gas region near the burner rim.

The impact of assuming constant composition on the measured temperature is assessed by comparing the temperatures obtained for three different Gladstone-Dale constants ($R_G$): $R_G = R_{G,air}$ (the reference case), $R_G$ equal to that of burnt gases ($R_G = R_{G,burnt}$), and $R_G$ equal to that of the fresh mixture, ($R_G = R_{G,fresh}$). **Figure 12** illustrates the results for the case depicted in **figure 5** by comparing the temperature profiles at $h = 1.2D$ obtained using the three different $R_G$ values. While $R_{G,air}$ and $R_{G,burnt}$ are nearly equal, resulting in minimal differences in their corresponding temperature profiles, the temperature profile computed with $R_{G,fresh}$ is significantly lower, **figure 12a**. In both cases, the maximum absolute temperature difference is found in the flame region, where the highest temperature is located. The maximum absolute error committed by assuming a constant composition is $\Delta T_{MAX}^{R} \cong -35°C$ in the fresh mixture region (inside the flame cone), and $\Delta T_{MAX}^{R} \cong 27°C$ in the burnt gases region, (between the flame cone and the plume). The relative temperature differences, **figure 12b,** show a constant value of approximately 2% for the burnt gases and about 9% for the fresh mixture across the entire domain.

The uncertainty in the mean displacements is given by the standard deviation computed from the 100 displacement maps, and in the object space its maximum value corresponds to approximately $0.2\ mm$, which translates to a maximum uncertainty in the temperature measurements of $\Delta T_{MAX}^{displ} = 4°C$.The uncertainty increases at higher flame heights, where the displacement maps show higher variance due to the flame fluctuations and turbulence. However, such temperature uncertainty is almost negligible compared to those originating from the other two sources of uncertainty.

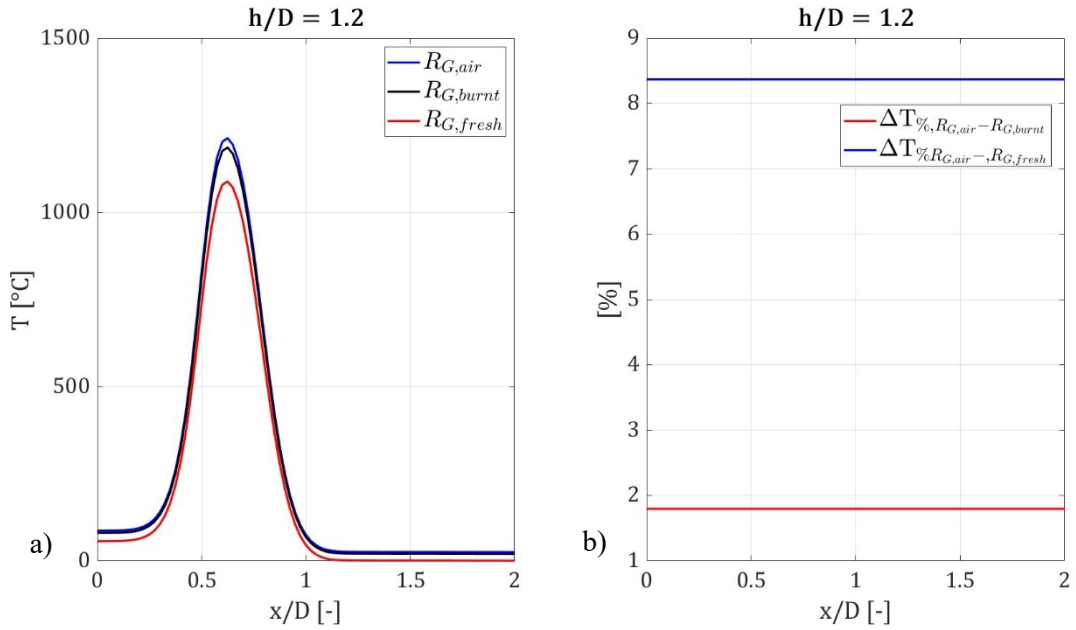


**Figure 12.** a) Mean temperature profiles computed with $R_{G,air}$, $R_{G,burnt}$ and $R_{G,fresh}$at $h = 1.2D$. b) Percentage mean temperature difference between the case computed with $R_{G,air}$ and the cases computed with $R_{G,fresh}$ and $R_{G,burnt}$.

Summing up the three contributions, the resulting uncertainty of the tomographic BOS in the exhaust gas region is computed with formula (14):

$$\Delta T_{MAX}^{tomoBOS} \approx \sqrt{\left(\varepsilon_{\Delta T}^{Z_d}\right)^2 + (\Delta T_{MAX}^{R})^2 + \left(\Delta T_{MAX}^{displ}\right)^2} \approx 40[°C] \quad (14)$$

This finding implies that in order to minimize the uncertainty associated with the technique, efforts should be directed towards refining the method used to measure the distance from the burner to the background, as well as gaining a comprehensive understanding of the composition variations within the mixture.

## 7. Conclusions

Background Oriented Schlieren (BOS) is a Line-of-Sight (LoS) optical technique that allows to visualize and measure density gradients within transparent media. It relies on the relationship between fluid density and refractive index. In this particular study, the BOS technique together with an innovative deconvolution algorithm called ARAP (Arbitrary Ray Axisymmetric Projection) is employed to examine a premixed axis-symmetric hydrogen flame with the aim of quantitatively estimating the refractive index and the temperature distributions. The ARAP technique is favored over Abel-based methods because it allows to model light rays according to the pinhole camera model. Density gradients and temperature distribution are evaluated assuming ideal gas behavior and constant composition in isobaric conditions.

Since the ARAP transform requires specifying the regularization parameter and the discretization step, the study aims to assess the influence of these parameters on the solution and how to appropriately select them.

A regularization parameter of $\lambda = 75$ was chosen along with $N_r = 125$ and $N_x = 250$ to prevent excessive signal filtering and avoid excessive temperature gradients smoothing. With these parameters, refractive index and temperature maps were determined.

Temperature profiles were extracted at various heights from the Bunsen burner rim and compared with thermocouple measurements. As the extraction height increases, thermocouple measurements approach the temperature profiles obtained with tomographic BOS technique. Temperatures measured near the Bunsen axis were significantly higher than calculated temperatures, closely resembling adiabatic flame temperatures under experimental conditions. This discrepancy may be attributed to the catalytic effect of platinum in the thermocouple junction, which, being preheated by exhaust gases, ignites the hydrogen-air mixture before reaching the flame front.

A simplified quantification of tomographic BOS uncertainty considering only the contributions from Bunsen distance measurement uncertainty, assumption of constant composition, and statistical uncertainty of the mean displacement, revealed that the former two factors contributed significantly more to the overall uncertainty. This highlights the need for refinement in Bunsen distance measurement and further methods to address mixture composition variability. The resulting maximum uncertainty, found in the exhaust gas region, was estimated to be about $40\ °C$.

## References

[1] Venkatakrishnan L and Meier G E A 2004 Density measurements using the Background Oriented Schlieren technique *Exp Fluids* **37** 237–47

[2] Goldhahn E and Seume J 2007 The background oriented schlieren technique: Sensitivity, accuracy, resolution and application to a three-dimensional density field *Exp Fluids* **43** 241–9

[3] Nicolas F, Todoroff V, Plyer A, Le Besnerais G, Donjat D, Micheli F, Champagnat F, Cornic P and Le Sant Y 2016 A direct approach for instantaneous 3D density field reconstruction from background-oriented schlieren (BOS) measurements *Exp Fluids* **57** 1–21

[4] Cozzi F, Göttlich E, Angelucci L, Dossena V and Guardone A 2017 Development of a background-oriented schlieren technique with telecentric lenses for supersonic flow *Journal of Physics: Conference Series* vol 778 (Institute of Physics Publishing)

[5] Venkatakrishnan L and Meier G E A 2004 Density measurements using the Background Oriented Schlieren technique *Exp Fluids* **37** 237–47
[6] Cozzi F, Colombo L P M, Lucchini A, Coghe A, Muzzio A and Pacini F 2010 Background Oriented Schlieren characterization of the thermal boundary layer over a vertical heated plate in free convection *XVIII AIVELA National Meeting* (Roma)
[7] Ramaiah J, de Rubeis T, Gannavarpu R and Ambrosini D 2023 Quantitative flow visualization by hidden grid background oriented schlieren *Opt Lasers Eng* **160**
[8] Ambrosini D, Rubeis T De, Paoletti D, Ramaiah J and Gannavarpu R 2023 Hidden Grid Background Oriented Schlieren in studying convective flows *Journal of Physics: Conference Series* vol 2509 (Institute of Physics)
[9] Iffa E D, Aziz A R A and Malik A S 2011 Gas Flame Temperature Measurement Using Background Oriented Schlieren *Journal of Applied Sciences* **11** 1658–62
[10] Grauer S J, Unterberger A, Rittler A, Daun K J, Kempf A M and Mohri K 2018 Instantaneous 3D flame imaging by background-oriented schlieren tomography *Combust Flame* **196** 284–99
[11] Choudhury S P and Joarder R 2022 High-speed photography and background oriented schlieren techniques for characterizing tulip flame *Combust Flame* **245**
[12] Iapaolo F and Cozzi F 2023 Density gradient measurement of a premixed hydrogen-air flame with Background Oriented Schlieren technique *Proceedings of the 11th European Combustion Meeting 2023* pp 910–4
[13] Settles G S and Hargather M J 2017 A review of recent developments in schlieren and shadowgraph techniques *Meas Sci Technol* **28**
[14] Raffel M 2015 Background-oriented schlieren (BOS) techniques *Exp Fluids* **56** 1–17
[15] Raffel M, Willert C E, Scarano F, Kähler C J, Wereley S T and Kompenhans J 2018 *Particle Image Velocimetry* (Springer Cham)
[16] Atcheson B, Heidrich W and Ihrke I 2009 An evaluation of optical flow algorithms for background oriented schlieren imaging *Exp Fluids* **46** 467–76
[17] Rajendran L K, Bane S P M and Vlachos P P 2019 Dot tracking methodology for background-oriented schlieren (BOS) *Exp Fluids* **60**
[18] Tokgoz S, Elsinga G E, Delfos R and Westerweel J 2012 Spatial resolution and dissipation rate estimation in Taylor-Couette flow for tomographic PIV *Exp Fluids* **53** 561–83
[19] Sourgen F, Haertig J and Rey C 2004 Comparison between background oriented schlieren measurements (B.O.S.) and numerical simulations *24th AIAA Aerodynamic Measurement Technology and Ground Testing Conference*
[20] Sourgen F, Leopold F and Klatt D 2012 Reconstruction of the density field using the Colored Background Oriented Schlieren Technique (CBOS) *Opt Lasers Eng* **50** 29–38
[21] Venkatakrishnan L 2005 Density measurements in an axisymmetric underexpanded jet by background-oriented schlieren technique *AIAA Journal* **43** 1574–9
[22] Venkatakrishnan L and Suriyanarayanan P 2009 Density field of supersonic separated flow past an afterbody nozzle using tomographic reconstruction of BOS data *Exp Fluids* **47** 463–73
[23] Sipkens T A, Grauer S J, Steinberg A M, Rogak S N and Kirchen P 2022 New transform to project axisymmetric deflection fields along arbitrary rays *Meas Sci Technol* **33**
[24] Dasch C J 1992 One-dimensional tomography: a comparison of Abel, onion-peeling, and filtered backprojection methods *Appl Opt* **31** 1146
[25] Kolhe P S and Agrawal A K 2009 Abel inversion of deflectometric data: comparison of accuracy and noise propagation of existing techniques *Appl Opt* **48** 3894
[26] Cakir B O, Lavagnoli S, Saracoglu B H and Fureby C 2023 Assessment and application of optical flow in background-oriented schlieren for compressible flows *Exp Fluids* **64**
[27] Vinnichenko N A, Uvarov A V and Plaksina Y Y 2012 Accuracy of background oriented schlieren for different background patterns and means of refraction index reconstruction *15th International Symposium on Flow Visualization* (Minsk)

[28] Merzkirch W 1987 *Flow Visualization* (Academic Press)
[29] Gardiner W C, Hidaka Y and Tanzawa T 1981 *Refractivity of Combustion Gases* vol 40
[30] Davidson T A 1993 *A Slmple and Accurate Method for Calculatlng Viscosity of Gaseous Mixtures I UNITED STATES DEPARTMENT OF THE INTERIOR I*
[31] Xiong Y, Kaufmann T and Noiray N 2020 Towards robust BOS measurements for axisymmetric flows *Exp Fluids* **61**
[32] Paraschiv L S, Serban A and Paraschiv S 2020 Calculation of combustion air required for burning solid fuels (coal / biomass / solid waste) and analysis of flue gas composition *Energy Reports* vol 6 (Elsevier Ltd) pp 36–45
[33] Taylor J R 1997 *An Introduction to Error Analysis* (Sausalito, California: University Science Books)

**Acknowledgments**
A special thank goes to Dr. Thimoty A. Sipkens for his support and guidance in implementing the ARAP transform.
Project funded under the National Recovery and Resilience Plan (NRRP), Mission 4 Component 2 Investment 1.3 - Call for tender No. 1561 of 11.10.2022 of Ministero dell'Università e della Ricerca (MUR); funded by the European Union – NextGenerationEU - Project code PE0000021, Concession Decree No. 1561 of 11.10.2022 adopted by Ministero dell'Università e della Ricerca (MUR) – Project title "Network 4 Energy Sustainable Transition – NEST".